

## FAILURE MECHANISM OF AN EMBANKMENT RESTING ON LIQUEFIABLE GROUND

Tetsuo TOBITA<sup>1</sup> and Susumu IAI<sup>2</sup>

### ABSTRACT

It is empirically known that the amount of residual crest settlement of an embankment resting on liquefiable ground depends on the intensity of input motion. To properly estimate crest settlements after large earthquakes, the failure mechanism has to be clearly addressed. Based on the results of centrifuge experiments and numerical analysis, the failure mechanism of an embankment on liquefiable ground is investigated. The embankment is made of dry sand underlain by a deposit of loose saturated sand. The model is subjected to sinusoidal input motion with various peak acceleration amplitudes. The effective stress analysis, then, simulates well the overall behavior of the experimental counterparts. By the numerical analysis, formation of a non-liquefied wedge under the embankment is observed. Also its size is found to be positively correlated with the amount of settlement. Measured pore water pressure buildup curves just under the embankment confirm the existence of non-liquefied area at the beginning of shaking. In addition to the above experiments and numerical analysis, the static loading model tests with liquefaction by sand boiling are conducted. The test resulted in a positive correlation between the size of non-liquefied wedge and inclination angle. While the analytical solution of inclined distributed load on the infinite elastic half-space shows a development of shallow failure mechanism with an increase in the horizontal component of distributed load. Failure mechanism of the liquefiable ground under overburden pressure is confirmed to be different from that of dry sand.

Keywords: Earthquake, Liquefaction, Embankment, Failure mechanism

### INTRODUCTION

During large earthquakes, liquefaction-induced ground deformation often causes extensive damage on structures. The phenomena are complex and involve large strain. To simulate such a large deformation, various effective stress constitutive models have been proposed (e.g., Martin, et al., 1975; Iai, et al., 1992; Prevost, 1998; Oka, et al., 1999; Yasuda, et al., 1999; Tobita and Bardet, 2003). Several numerical simulation models, thus, have been developed and reasonable results have been obtained through comparison with real earthquake damage or centrifuge model tests. However, such a detailed analysis is time consuming and not economical, and only applied to the verification of designs of some important structures.

Conventional seismic design for embankments has been done by pseudo-static limit equilibrium analysis, sometimes combined with a sliding-block analysis (Newmark, 1965). These methods have been widely used due to their simplicity. However, with recent water-front developments and urban sprawl, many liquefaction-induced damage have been reported on earthdams and river dikes after large earthquakes (Seed, et al., 1975, Seed, et al., 1990, Bardet and Davis, 1996, Matsuo, 1996,

---

<sup>1</sup> Assistant professor, Disaster Prevention Research Institute, Kyoto University, Japan, Email: tobita@geotech.dpri.kyoto-u.ac.jp

<sup>2</sup> Professor, Disaster Prevention Research Institute, Kyoto University, Japan, Email: iai@geotech.dpri.kyoto-u.ac.jp

Ozutsumi, et al., 2002, Nishimoto, 2003). Although, the damage associated with liquefaction-induced deformation indicates a limitation of conventional pseudo-static design method, simplified design methods are still required for practice. Such a simple but accurate method based on the deep understanding of failure mechanism of an embankment resting on liquefiable sandy deposit can alternatively be used to verify results of detailed numerical analysis.

The objective of the present study is to investigate the failure mechanism of an embankment resting on the liquefiable ground. Especially we will look into the deformation mechanism of liquefied ground under an embankment. The results of centrifuge tests and effective stress analysis which have been reported in Tobita, et al., (2006) are reinvestigated to study the failure mechanism in detail. In addition to these experiments and numerical studies, static loading model tests with liquefaction by sand boiling is conducted to visualize the formation of a non-liquefied wedge under an embankment.

## MEASURED AND COMPUTED DEFORMATION OF THE EMBANKMENT

### Centrifuge experiments

Experiments were conducted in a rigid wall container mounted on 2.5 m radius geotechnical centrifuge at the Disaster Prevention Research Institute, Kyoto University (DPRI-KU). Overall dimensions of the rigid container are  $450 \times 150 \times 300$  mm in length, width, and height, respectively (Figure 1). Dynamic excitation was given in the direction parallel to the cross-section shown in Figure 1. The applied centrifugal acceleration was 50 G. In what follows, the units are for the prototype, if not otherwise specified.

A cross-section of the model embankment resting on a deposit of saturated sand is depicted in Figure 1. The crest height was 3.0 m, lateral lengths at the top and bottom were 4.0 and 11.5 m, respectively, and the side slope was set to be 1:1.25 scale. Silica sand ("Soma" sand No. 5) ( $e_{\max} = 1.11$ ,  $e_{\min} = 0.69$ , and  $D_{50} = 0.38$  mm) was used for both the deposit and embankment. Only the deposit was saturated with viscous fluid with viscosity of 50 cSt (50 times that of water). Crushed stones (approx.  $\phi = 10$  mm) were placed at the base of the embankment to prevent the embankment from soaking up pore water by suction.

Three tests with loose sand deposit were conducted by changing the maximum amplitude of the input acceleration (Table 1). Loose saturated sand deposits were prepared by water pluviation of sand to the target relative densities of about 30% in about 100 mm lifts (model scale). The embankment was made of dry sand with relative density approximately 70%. Before adding the sand, rehydratable noodles were attached to the inner side of the glass wall installed in one of the side walls of the container, which would visualize the ground deformation with depth. After setting up the model, a centrifugal force of 50 G was applied for approximately 5 min for consolidation, and then the machine was stopped to measure the height of the deposit and embankment with a ruler to obtain the exact value of the relative density. Input acceleration was given by 1 Hz sinusoidal waves over 20 cycles.

**Table 1. Summary of test cases**

Case	Soil type	Relative density Dr (%)	Max. input acceleration (m/s <sup>2</sup> )	Residual crest Settlements (m)
1	Loose	27	0.81	0.01
2		30	1.79	1.00
3		30	3.13	1.40

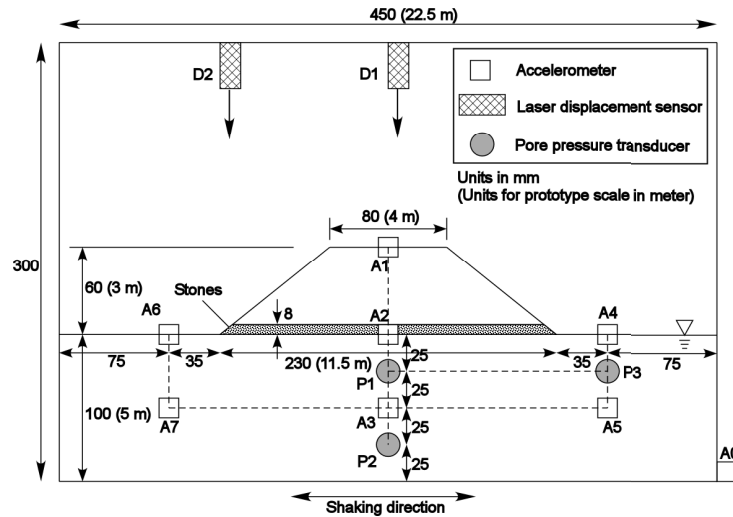


**Figure 1. Model configuration in rigid container.**

### Numerical analysis

The results of effective stress analysis by FLIP (Finite element analysis for Liquefaction Process) (Iai, et al., 1992) are compared with the experimental results. Modeling parameters are defined in Tables 2 and 3. As a result of the lack of detailed laboratory data for the sand used in the centrifuge tests, these parameters were determined by the empirical relationship with the values of the corrected SPT blow counts,  $N_{65}$ , which is the adjusted blow counts corresponding to an effective overburden stress of 65 kPa (Morita, et al., 1997). As shown later, the parameters corresponding to blow counts of  $N_{65} = 1$  for the loose deposit gave the best match with the experimental results. Model parameters for the embankment are determined by assuming  $N_{65} = 40$ . These blow counts were confirmed to be within the range of the existing correlations with relative densities (e.g., Skempton, 1986).

**Table 2. Model parameters for deformation properties.**

Soil Type	Corrected SPT Blow count, $N_{65}$	Parameter for deformation characteristic									
		Density	Porosity	Elastic tangent shear modulus at $p_r$	Elastic tangent bulk modulus at $p_r$	Reference mean effective stress	Poisson ratio	Exponent of a power function for modulus	Internal friction angle	Cohesion	Max. damping ratio
		$\rho$ $\times 10^3$ (kg/m <sup>3</sup> )	$n$	$G_r$ $\times 10^5$ (kPa)	$K_r$ $\times 10^5$ (kPa)	$p_r$ (kPa)	$\nu$	$m$	$\phi_f$ (°)	$c$ (kPa)	$h_{max}$
Loose	1	1.34	0.498	0.1987	0.5182	98.0	0.33	0.50	37.5	0.0	0.24
Embankment	40	1.45	0.450	1.885	4.916				43.3		

**Table 3. Model parameters for liquefaction properties.**

Soil Type	Corrected SPT blow count, $N_{65}$	Parameter for liquefaction characteristic						
		Phase trans. Ang.	Parameters for dilatancy					
			$\phi_p$ (°)	$w_1$	$p_1$	$p_2$	$c_1$	$S_1$
Loose	1	28.0	3.507	0.50	1.109	0.773	0.005	
Dense	40	28.0	21.40	0.50	0.407	13.26	0.005	

### Experiments versus numerical simulation

The measured and computed embankment deformations of two cases (Case 2, 3) are depicted in Figure 2. In Figure 2, only the upper 50 mm (model scale) of the cross-section of the experiments was delineated from photographs taken after shaking, because the lower 50 mm (model scale) of the cross-section was hidden behind the container wall.

For Case 2 in Figure 2(a), although the deposit was laterally expanded due to the weight of the embankment under strong shaking, the body of the embankment was vertically settled and kept its original shape. Measured residual crest settlement was 1 m, and computed settlement was 0.89 m. In both measured and computed deformation, soils near the toes were laterally pushed in the direction opposite to the embankment and slightly uplifted, while soils under the embankment were compressed vertically and expanded laterally with shear.

For Case 3 in Figure 2(b), the body of the embankment was laterally expanded along with the failure arc, and its shoulders were more deformed than that of Case 2. The computed shape after shaking in the figure is in agreement with its experimental counterpart. The residual crest settlements were coincidentally 1.4 m (47% of its original height) in both measured and computed settlements. However, the amount of settlement was out of the range of the LDT during the experiment and, therefore, it was obtained by subtracting the measured height of the embankment before shaking from that after the shaking. As shown in Figure 3(a), not only the amount of settlement after the shaking but also the transient motion during shaking were properly simulated. The crest acceleration of the first few cycles shown in Figure 3(a) is overestimated, but the amplitude after 5 s agrees well. The time histories of computed settlements (up to 8 s) and pore water pressure build-up shown in Figure. 3(b and c) are also consistent with measured values.

The amount of residual crest settlement is regarded as one of the measures for the seismic performance of an embankment. The measured and computed seismic performance against the peak input acceleration is shown in Figure 4. The curve indicates a positive correlation between these two components; the increase in the input acceleration amplitude causes large crest settlement. Although the amount of settlement is consistently increasing with the increase in the input acceleration in the present study, past case histories indicate that the maximum amount of settlement may be bounded at large input accelerations. In Figure 4, three computational results with model parameters corresponding to  $N_{65}$  of 1, 3, and 5, are shown for comparison. Among these computations, results for the case of  $N_{65} = 1$  are in reasonable agreement with the experimental results.

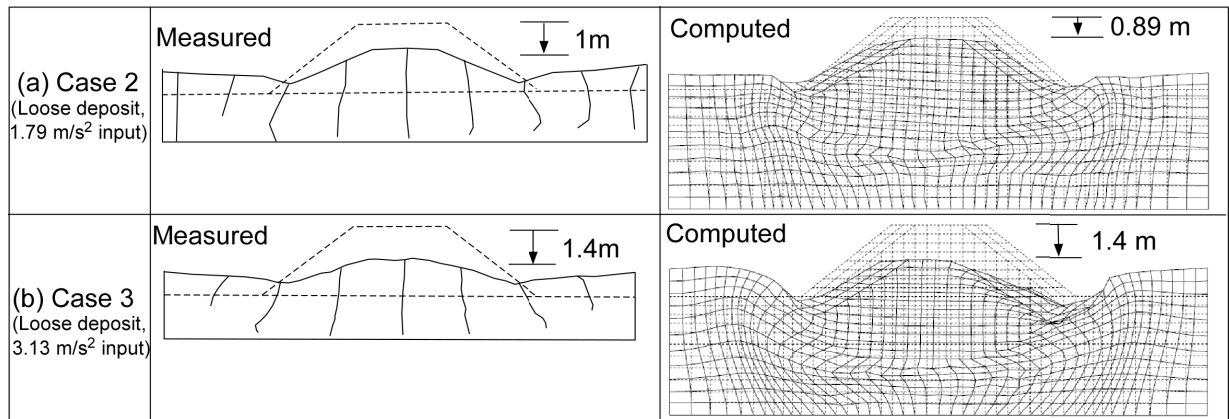


**Figure 2. Measured and computed deformation of the embankment: (a) Case 2, (b) Case 3,**

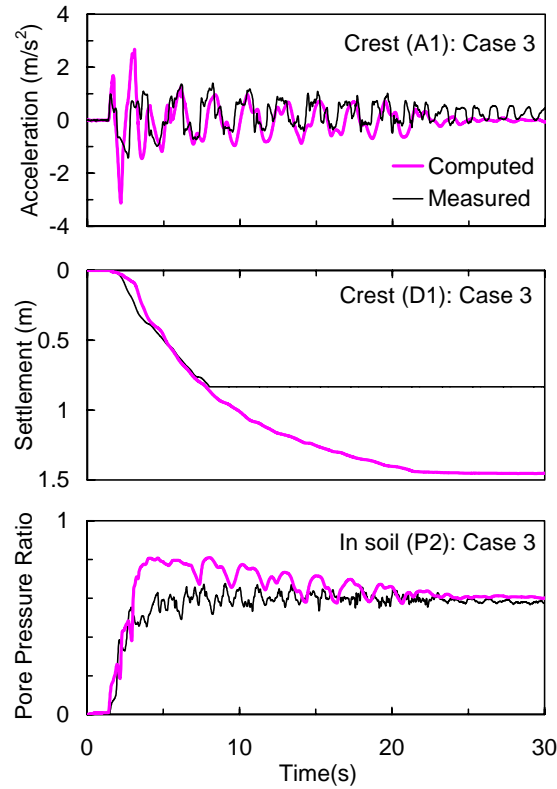


**Figure 3. Time histories of crest acceleration at the crest (A1), crest settlement at the crest (D1), excess pore water pressure ratio (P2) for Cases 3**

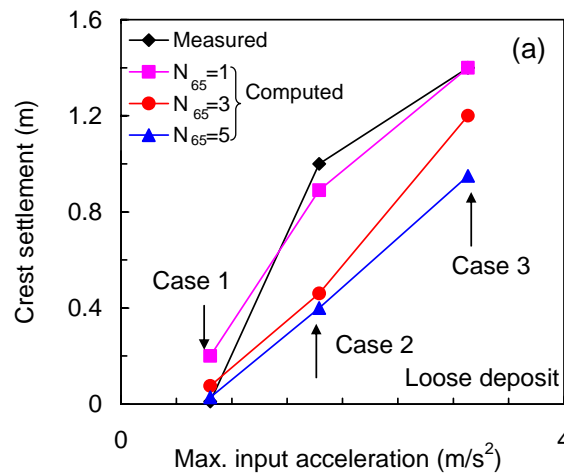


**Figure 4. Seismic performance of the embankment: Residual crest settlement versus maximum input acceleration**

### DEFORMATION MECHANISM OF THE EMBANKMENT ON LIQUEFIED SAND DEPOSIT

The deformation mechanism of an embankment on a loose saturated sand deposit subjected strong shaking is investigated in this section. From the earlier discussions, it is clear that (1) crest settlement resulted from compression in the vertical and extension in the lateral directions of a deposit under the

embankment, and (2) the amount of residual crest settlement depends on the intensity of the input acceleration.

The amount of crest settlement due to deformation of the deposit may be governed by the following factors: (a) the weight of the embankment as a dead load, (b) the bearing capacity and number of cyclic shear stresses applied to the deposit, (c) the degree of liquefaction that can be measured by the excess pore water pressure ratio and/or the duration of liquefaction, and (d) the inertial force acting on the embankment. Among these factors, (d) is directly related to the intensity of the input acceleration. The crest acceleration (see Figure 5) of Case 3 was slightly larger than that of Case 2 up to 5 s (i.e., before liquefaction), and after 5 s, the acceleration amplitude was attenuated and became the same level. This may imply that the amount of crest settlement is largely affected by the intensity of acceleration at the beginning of shaking.

Transient motions of the deformation and excess pore water pressure ratios at the specific times indicated by (A–F) in Figure 5 are shown in Figure 6. The areas of low pore water pressure ratio (non-liquefied area) are identified as areas with darker color (blue) in the deposit. These figures show that the area of low pore water pressure in Case 3 is larger than that in Case 2. This contradicts the general conclusion that the larger the input motion is, the more the soil is liquefied.

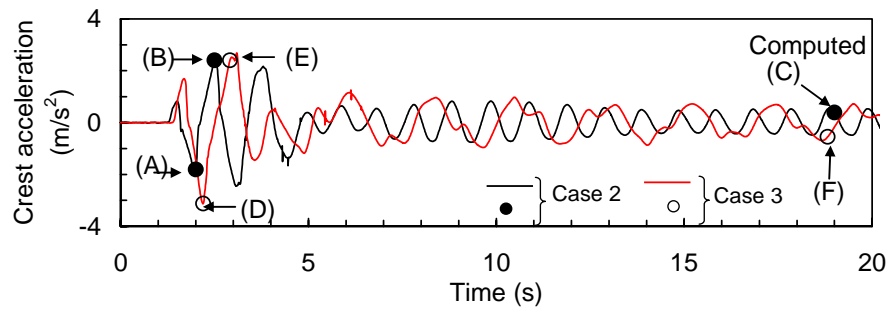


**Figure 5. Crest acceleration for Cases 2 and 3. Markers indicate the time shown in Fig. 6.**

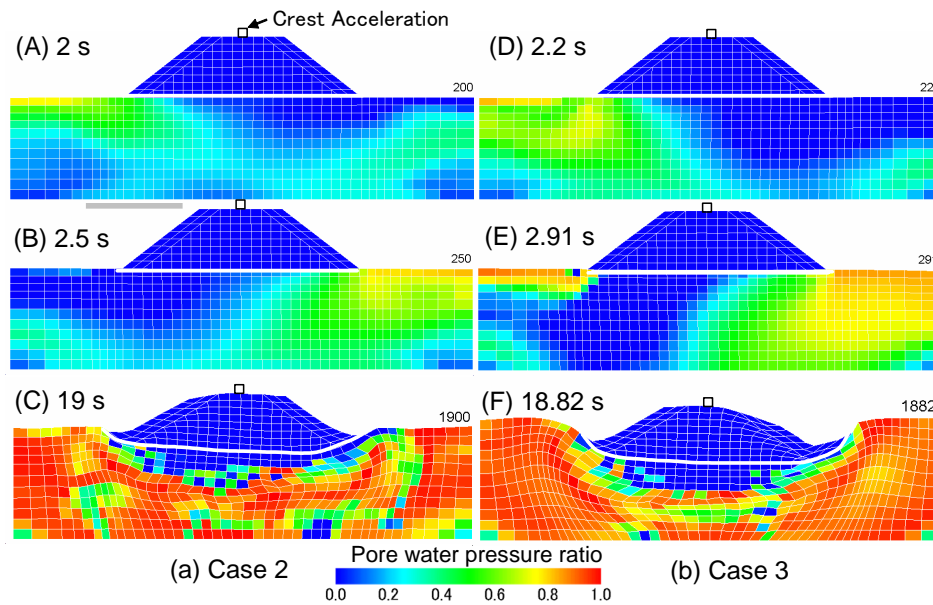


**Figure 6. Deformed shape and excess pore water pressure ratio at various time steps indicated by (A–C) for Case 2 and (D–F) for Case 3.**

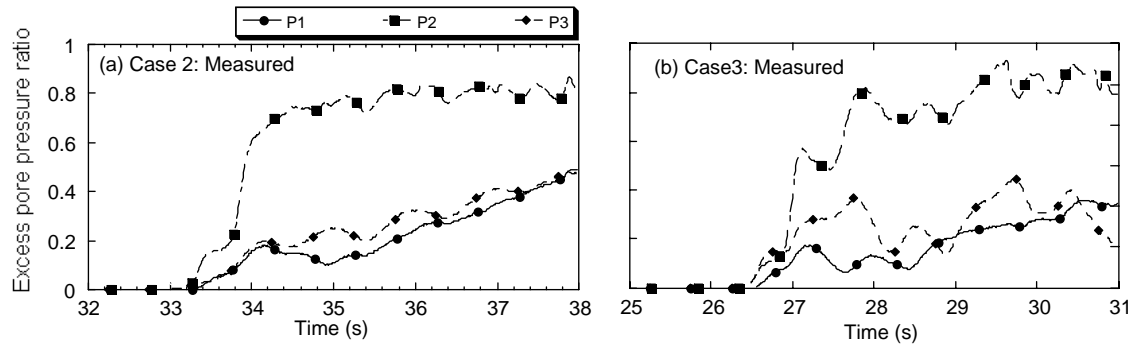


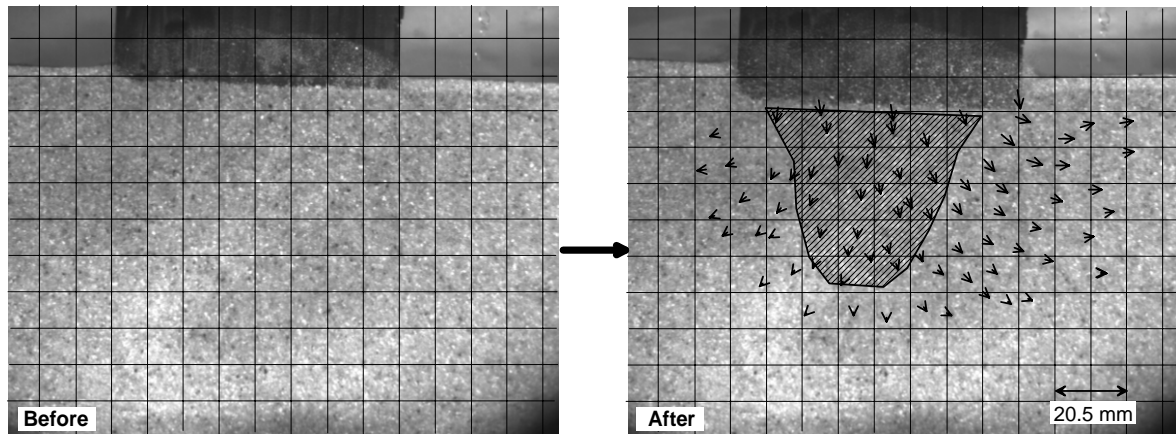
**Figure 7. Time histories of excess pore pressure ratio for loose saturated deposit in the centrifuge experiments shown in Figure 1: (a) Case 2 and (b) Case 3.**

The important factor causing this type of deformation mechanism may be the high contrast of shear strength between the non-liquefied and liquefied deposits. The soil just under the embankment suffers from larger overburden pressure due to the weight of the embankment than that of a deposit in the free field. The rate of excess pore water pressure build-up in the deposit under the embankment is slower than that in the free field. To see the delay of the pore water pressure buildup in the centrifuge tests, Figure 7 compares the time histories for Cases 2 and 3. In both cases, the pore pressure ratio under the embankment (P1) is consistently lower than that in the free field (P3) at the beginning of shaking. As seen in Figure. 7(b), the pore pressure ratio of P3 is four times larger than that of P1 at the maximum difference. If we assume that the shear modulus is proportional to the square root of the pore pressure ratio, the deposit may have twice the difference in shear strength.

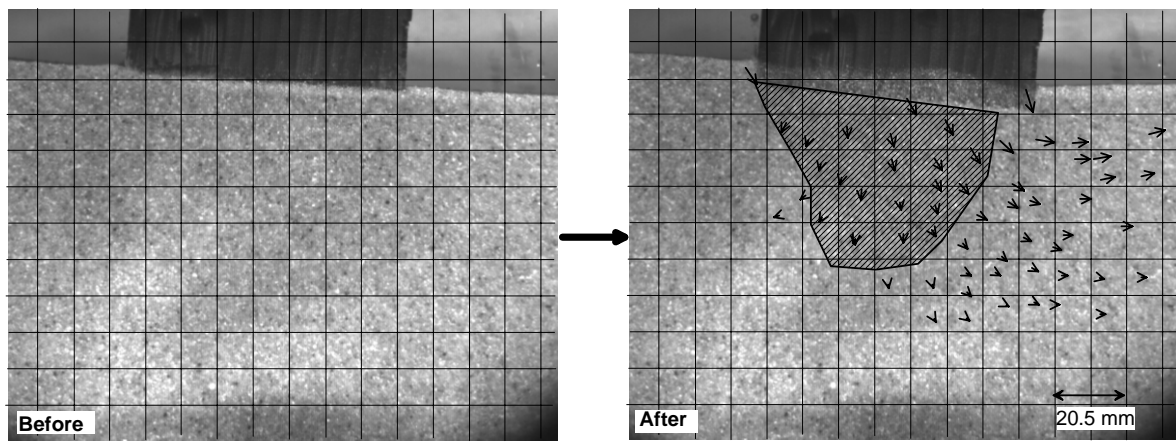
#### **Formation of the non-liquefied wedge under the static loading tests**

A series of model tests were conducted to visualize the formation of the non-liquefied wedge mentioned in the previous section and the deformation processes of the liquefied ground. The model ground was prepared in the sand box made of acrylic boards whose dimension was  $300 \times 50 \times 300$  mm in length, width, and height. The water inlet tubes were installed at the bottom of the box so that liquefaction by the sand boiling could be generated. Overburden pressure was given by an aluminium block whose dimension was  $82 \times 50 \times 41$  mm in length, width, and height, and weight of 0.42 kg. By inclining the box, the static load can be applied laterally to the model. Test procedures are as follows; (1) Silica sand ( $e_{\max}=1.0$ ,  $e_{\min}=0.76$ ) was pored into the box, then the loose deposit was made by sand boiling and adjusting the height of the ground surface of 215 mm from the bottom of the box, (2) To give the overburden pressure, the aluminium block was placed at the surface of the model ground, (3) The box was slowly inclined until specified inclination was achieved. In the present study, the inclination angle of 2.6, 3.9 and 6.5 degrees were specified, (4) The quantity of water flow was increased until the block was displaced due to liquefaction. Several tests of the same inclination angle were repeated to see the deformation of the ground on average. In the experiments, reduction of the gravitational force by the inclination was 0.6% ( $=1-\cos(6.5)$ ) at the maximum inclination, and, therefore, regarded to be negligible.

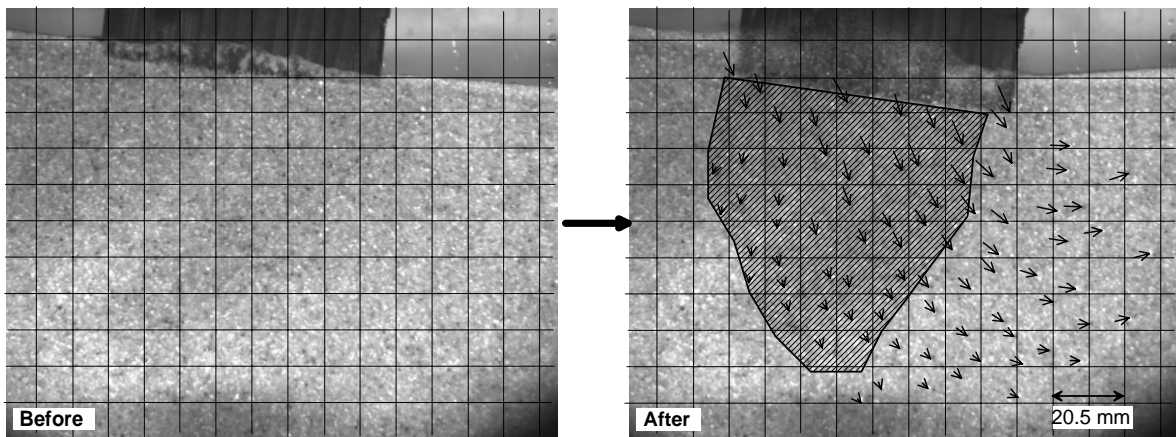
The deformation processes were captured by a high speed digital camera for the image processing. Photographs shown in Figure 8a to 8c are the ones before and after the deformation. Displacement vectors in these figures are obtained by comparing the images before and after the deformation. The shaded area under the aluminium block in Figure 8a to 8c is the area where the direction of the displacement vectors is less than 45 degrees from the vertical. At the beginning of deformation, soils under the overburden pressure were vertically compressed, and the compressed area formed the non-liquefied wedge. Then the wedge started to move downward and pushed liquefied ground in front of it. This process was seen commonly in all cases. However, a size of the wedge formed in the case of



(a) Surface slope: 2.6 degrees



(b) Surface slope: 3.9 degrees



(c) Surface slope: 6.5 degrees

**Figure 8a-c. Deformation of the ground under the overburden pressure with the initial ground slope of (a) 2.6, (b) 3.9, and (c) 6.5 degrees.**

the large inclination angle was larger than that of the small inclination. This trend is similar to the size of the area of low excess pore pressure ratio observed in the numerical analysis shown in Figure 6. From the test results, it may be concluded that the compression of the ground just under the overburden pressure is the major factor contributing to the formation of the non-liquefied wedge, and the size of the wedge may be positively correlated with the amount of deformation.



In general, the bearing capacity of soils decreases with the increase in lateral loads, because the failure surface becomes shallower (see appendix). This is true if the deposit is homogeneous, that is, the surrounding soil has the same stiffness as the mobilized wedge. On the other hand, if the surrounding soil loses its stiffness such as in the case of the liquefied deposit near the toe of the embankment, a non-liquefied wedge under the embankment may penetrate into the surrounding soft soils. If this is a case of dynamic excitation, larger input motion may produce a larger failure surface. Therefore, the amount of residual crest settlement depends not only on the number of applied stress cycles and the degree of liquefaction and so forth but also on the size of the non-liquefied wedge formed at the beginning of shaking. This mechanism may explain why the compacted area underneath an embankment is an effective countermeasure for deformation due to liquefaction.

## CONCLUSIONS

Failure mechanism of the embankment whose height was 3m was investigated in detail by the centrifuge tests and the effective stress analysis. As a result of the numerical analysis, an area of low excess pore pressure (non-liquefied area) was observed at the beginning of shaking, and it moved left or right as shaking continued. The area of low excess pore pressure was larger when the amplitude of input acceleration is larger. The formation of the area was indicated also by the observed time history of excess pore water pressure during the centrifuge experiments. At the beginning of shaking, the excess pore water pressure just under the embankment was consistently smaller than that of free field, and as shaking continued, both records reached complete liquefaction. To visualize the formation process of the non-liquefied area, model tests were conducted with a small sand box. In the box, to give an overburden pressure, an aluminum block was placed on top of a deposit of loose saturated sand. Then, the box was inclined to give lateral static force to the model and water was supplied from the bottom of the box to generate excess pore water pressure, i.e., liquefaction by sand boiling. The deformation process recorded by a high speed camera showed that initially, just after the liquefaction, sands under the overburden pressure were compressed vertically to form non-liquefied wedge. Then the wedge moved downward to push liquefied sands in front of it. Size of the wedge was larger as the inclination of the box, i.e., lateral force, became larger. This fact is consistent with the formation of the non-liquefied wedge in the numerical analysis mentioned above. Thus, the non-liquefied area in liquefied ground gives large influence on the deformation of peripheral ground, and the size is strongly correlated with the amount of deformation.

## APPENDIX

### Stresses under inclined distributed load in the infinite elastic half space

Based on the derivation of the stresses due to point load by (Boussinesq, 1885), stresses caused by strip area carrying inclined uniform pressure (Figure 9) is derived. The magnitude of uniform pressure is represented by  $q = \rho gh\sqrt{1+k_h^2}$ , and the inclination of the uniform pressure is set as  $\alpha = \tan^{-1}(k_h)$ , where  $\rho$  is density of soil,  $h$  is height of an embankment,  $g$  is acceleration due to gravity, and  $k_h$  is design seismic coefficient. Stresses due to small inclined point load,  $qdx$ , is given as,

$$d\sigma_z = -\frac{2qdx}{\pi z} \cos(\alpha + \psi) \cos^3 \psi \quad (1a)$$

$$d\sigma_x = -\frac{2qdx}{\pi z} \cos(\alpha + \psi) \cos \psi \sin^2 \psi \quad (1b)$$

$$d\tau_{xz} = -\frac{2qdx}{\pi z} \cos(\alpha + \psi) \sin \psi \cos^2 \psi \quad (1c)$$

where,  $x = z \tan \psi$ , therefore,  $dx = \frac{z}{\cos^2 \psi} d\psi$ . Substituting this into (1a) yields,

$$d\sigma_z = -\frac{2q}{\pi z} \cos(\alpha + \psi) \cos \psi d\psi \quad (2)$$

By taking integral from the angle of  $\beta_1$  to  $\beta_2$ ,

$$\sigma_z = -\frac{2q}{\pi} \int_{\beta_1}^{\beta_2} \cos(\alpha + \psi) \cos \psi d\psi$$

$$= -\frac{q}{\pi} \left[ \cos \alpha \{ \sin(\beta_2 - \beta_1) \cos(\beta_2 + \beta_1) + \beta_2 - \beta_1 \} - \sin \alpha \{ \sin(\beta_2 - \beta_1) \sin(\beta_2 + \beta_1) \} \right] \quad (3)$$

$$\sigma_z = -\frac{q}{\pi} \{ \cos \alpha (2\varepsilon + \sin 2\varepsilon \cos 2\phi) - \sin \alpha \sin 2\varepsilon \sin 2\phi \} \quad (4)$$

where  $\beta_1$  and  $\beta_2$  are replaced by  $2\varepsilon = \beta_2 - \beta_1$  and  $2\phi = \beta_2 + \beta_1$ . This is the vertical stress due to inclined uniform pressure. Similarly, lateral and shear stresses can be derived from Eqs. (1b-1c),

$$\sigma_x = -\frac{q}{\pi} \left[ \frac{1}{2} \{ \cos \alpha (2\varepsilon - \sin 2\varepsilon \cos 2\phi) + \sin \alpha \sin 2\varepsilon \sin 2\phi \} + 2 \sin \alpha (\ln \cos \beta_2 - \ln \cos \beta_1) \right] \quad (5)$$

$$\tau_{xz} = -\frac{q}{\pi} \{ \sin \alpha (\sin 2\varepsilon \cos 2\phi - 2\varepsilon) + \cos \alpha \sin 2\varepsilon \sin 2\phi \} \quad (6)$$

Principal stresses are written by Eqs. (4-6),

$$\sigma_1 = \frac{1}{2} \left( \sigma_z + \sigma_x + \sqrt{(\sigma_z - \sigma_x)^2 + 4\tau_{xz}^2} \right) \text{ and } \sigma_3 = \frac{1}{2} \left( \sigma_z + \sigma_x - \sqrt{(\sigma_z - \sigma_x)^2 + 4\tau_{xz}^2} \right) \quad (7)$$

Therefore, the mean pressure plotted in Figure. 10 is expressed as,

$$\sigma_m = \frac{1}{2} (\sigma_1 + \sigma_3). \quad (8)$$

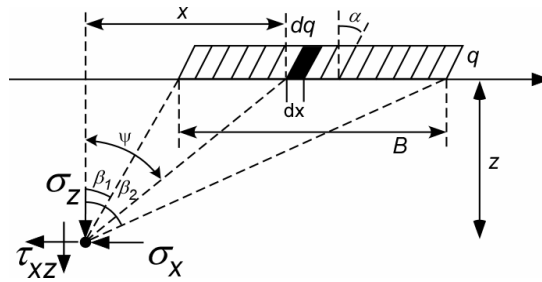
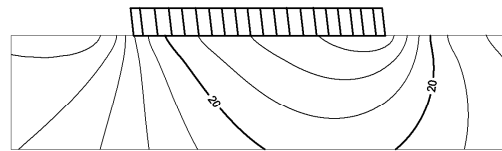
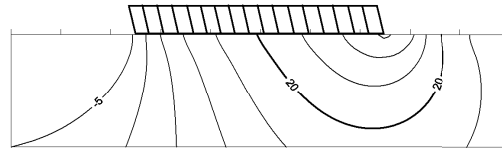


**Figure 9. Stresses due to inclined uniform pressure.**



(a) Analytical solution:  $kh=0.14$



(b) Analytical solution:  $kh=0.30$

**Figure 10. Contours of equal mean stress due to inclined distributed load by analytical solution**

## REFERENCES

- Martin, GR, Finn, WDL and Seed, HB. "Fundamentals of liquefaction under cyclic loading," Journal of Geotechnical Engineering, ASCE, 101, 5, 423-438, 1975.
- Iai, S, Matsunaga, Y and Kameoka, T. "Strain space plasticity model for cyclic mobility," Soils and Foundations, Japanese Society of Soil Mechanics and Foundation Engineering, 32, 2, 1- 15, 1992.

- Prevost, JH "DYNAFLOW: A Nonlinear Transient Finite Element Analysis Program," Princeton University, 1998.
- Oka, F, Yashima, A, Tateishi, Y, Taguchi, Y and Yamashita, S. "A cyclic elasto-plastic constitutive model for sand considering a plastic-strain dependence of the shear modulus," *Geotechnique*, 49, 5, 661-680, 1999.
- Yasuda, S, Yoshida, N, Adachi, K, Kiku, H and Gose, S. "A simplified analysis of liquefaction-induced residual deformation," *Proceedings of the 2nd International Conference on Earthquake Geotechnical Engineering*, 555-560, 1999.
- Tobita, T and Bardet, JP. "Energy-based liquefaction analysis of earthquake site response," *Proceedings of the Eighth U.S.-Japan Workshop on Earthquake Resistant Design of Lifeline Facilities and Countermeasures Against Liquefaction*, MCEER, 625-636, 2003.
- Newmark, NM "Effects of earthquakes on dams and embankments," *Geotechnique*, 15, 2, 139-160, 1965.
- Seed, HB, Lee, KL, Idriss, IM and Makdisi, FI. "The slides in the San Fernando Dams during the earthquake of February 9, 1971," *Journal of Geotechnical Engineering*, ASCE, 101, 7, 651-688, 1975.
- Seed, RB, Dickenson, SE, Riemer, MF, Bray, JD, Sitar, N, Mitchell, JK, Idriss, IM, Kayen, RE, Kropp, A, Hander, LFJ and Power, MS. "Preliminary Report on the Principal Geotechnical Aspects of the October 17, 1989, Loma Prieta Earthquake," Report No. UCB/EERC-90/05, Earthquake Engineering Research Center, University of California Berkeley, 1990.
- Bardet, JP and Davis, CA. "Performance of San Fernando dams during the 1994 Northridge Earthquake," *Journal of Geotechnical Engineering*, ASCE, 122, 7, 554-564, 1996.
- Matsuo, O. "Damage to river dikes," *Special Issue of Soils and Foundations*, Japanese Geotechnical Society, 235-240, 1996.
- Ozutsumi, O, Sawada, S, Iai, S, Takeshima, Y, Sugiyama, W and Shimazu, T. "Effective stress analysis of liquefaction-induced deformation in river dikes," *Soil Dynamics and Earthquake Engineering*, 22, 9-12, 1075-1082, 2002.
- Nishimoto, S "Damage on levees," Reconnaissance report on the 2003 Tokachi-oki, Japan, Earthquake, JSCE (in Japanese), <http://www.jsce.or.jp/>, 2003.
- Tobita, T, Iai, S and Ueda, K. "Dynamic Behavior of Sand Levee on Saturated Sand Deposits - Centrifuge and numerical studies-," 100th Anniversary Earthquake Conference Commemorating the 1906 San Francisco Earthquake April 18-22, 2006, at The Moscone Center, San Francisco, U.S.A., paper No. 1114, 2006.
- Morita, T, Iai, S, Liu, H, Ichii, K and Sato, Y. "Simplified method to determine parameter of FLIP," Technical Note of The Port and Harbour Research Institute, Ministry of Transport, Japan, 869, 36 (in Japanese), 1997.
- Skempton, AW. "Standard penetration test procedures and the effects in sands of overburden pressure, relative density, particle size, ageing and overconsolidation," *Geotechnique*, 36, 3, 425-447, 1986.
- Boussinesq, J. "Application des potentiels a L'etude de L'equilibre et du mouvement des solides elastiques," Gauthier-Villars, 1885.